Available online at www.sciencedirect.com

SCIENCE DIRECT®

ELSEVIER

European Journal of Mechanics B/Fluids 22 (2003) 221–237

Wall functions for numerical modeling of laminar MHD flows

Ola Widlund

CNRS-EPM, BP 95, 38402 St Martin d'Hères, France

Received 12 August 2002; received in revised form 1 April 2003; accepted 1 April 2003

Abstract

A general wall function treatment is presented for the numerical modeling of laminar magnetohydrodynamic (MHD) flows. The wall function expressions are derived analytically from the steady-state momentum and electric potential equations, making use only of local variables of the numerical solution. No assumptions are made regarding the orientation of the magnetic field relative to the wall, nor of the magnitude of the Hartmann number, or the wall conductivity. The wall functions are used for defining implicit boundary conditions for velocity and electric potential, and for computing mass flow and electrical currents in near wall-cells. The wall function treatment was validated in a finite volume formulation, and compared with an analytic solution for a fully developed channel flow in a transverse magnetic field. For the case with insulating walls, a uniform 20×20 grid, and Hartmann numbers $\mathrm{Ha} = \{10, 30, 100\}$, the accuracy of pressure drop and wall shear stress predictions was $\{1.1\%, 1.6\%, 0.5\%\}$, respectively. Comparable results were obtained also with conducting Hartmann walls. The accuracy of predicted pressure drop and wall shear stress was essentially independent of the resolution of the Hartmann layers. When applied also to the parallel walls, the wall functions reduced the errors by a factor two to three. The wall functions can be implemented in any general flow solver, to allow accurate predictions at reasonable cost even for complex geometries and nonuniform magnetic fields.

© 2003 Éditions scientifiques et médicales Elsevier SAS. All rights reserved.

1. Introduction

Laminar flows of electrically conducting fluids in a magnetic field are characterized by very thin boundary layers, especially so along walls perpendicular to the magnetic field. These boundary layers usually determine not only the total pressure drop, but also the overall velocity and electric current distributions in the core flow. The thickness of the boundary layers decrease with increasing magnetic field density, and in numerical simulations the required resolution of these boundary layers quickly becomes costly, even for rather modest magnetic fields.

A similar problem is encountered in the numerical simulation of high-Reynolds number turbulent flows, where the turbulent boundary layers are often too thin to be fully resolved at a reasonable cost. To avoid a costly numerical integration all the way into the viscous sublayer, one usually uses an analytic wall function (derived from the logarithmic "law of the wall") for interpolation between the first computational node and the wall (see, e.g., Launder and Spaulding [1]).

In this paper we propose a general wall function treatment for numerical modeling of laminar magnetohydrodynamic (MHD) flows.

A wall perpendicular to the magnetic field will develop a so-called Hartmann boundary layer, with thickness of order δ_H [2],

$$\delta_H \equiv \frac{1}{B}\sqrt{\frac{\mu}{\sigma}}, \tag{1}$$

E-mail address: widlund@grenoble.cnrs.fr (O. Widlund).

0997-7546/03/$ – see front matter © 2003 Éditions scientifiques et médicales Elsevier SAS. All rights reserved.
doi:10.1016/S0997-7546(03)00023-2

where B is the magnetic field density, μ is the fluid molecular viscosity, and σ its electric conductivity. This is the Hartmann distance, over which the viscous forces balance the magnetic forces. As a non-dimensional measure of the magnetic effects on the flow we take the Hartmann number,

$$\mathrm{Ha} \equiv \frac{h}{\delta_H} = \sqrt{\frac{\sigma}{\mu}} Bh, \tag{2}$$

where h is a characteristic length scale in the direction of the magnetic field. The dimensionless thickness of the Hartmann layers thus varies as Ha^{-1}. Along walls completely parallel to the magnetic field the distribution and balance of forces is different, and the thickness of the boundary layers can be shown to vary as $\mathrm{Ha}^{-1/2}$. These boundary layers are called side layers, or parallel layers. If the magnetic field has components both parallel and normal to the wall, the Hartmann layer behavior will usually dominate, and the wall-normal component B_n of the magnetic field replaces B in (1) and (2).

In numerical simulations of laminar MHD flows, the Hartmann layers can usually be resolved properly only for relatively low Hartmann numbers. For high Hartmann numbers, simulation algorithms described in the literature usually avoid resolving the Hartmann layers by assuming an exponential velocity profile between the bulk flow and the Hartmann walls. This approach is applicable only to the Hartmann layers, and is strictly valid only in the limit of high Hartmann numbers, for which one can show that the near-wall velocity in the Hartmann layer varies as

$$U(n) = U_c\big(1 - \exp(-n/\delta_H)\big), \tag{3}$$

if U_c is a well-defined core velocity, and n is the distance from the wall [2]. Given the gradient of electric potential in the core, the expression can be used to deduce also the transport of electric current in the Hartmann layer. This current is usually regarded as a thin current sheet at the wall boundary, and treated together with any current flowing in the wall itself. This high-Ha treatment of the Hartmann layers have been employed in a variety of different solver algorithms.

Bühler [3] developed a numerical procedure based on the inertia-less core approximation outlined by Kulikovskii [4]. It is assumed that the flow in the core is governed by a balance between the pressure and Lorentz forces. This requires that the Hartmann number is sufficiently large for viscous effects to be negligible outside very thin boundary layers, and further that the interaction parameter $N \equiv \sigma B^2 h/(\rho U_c)$ is large enough for Lorentz forces to dominate over inertial effects. Bühler included the effects of the viscous Hartmann layers using (3) and the related current distribution. The geometrical transformation used by Bühler suffers from a numerical singularity for walls parallel with the magnetic field. In some cases a separate treatment of these side layers allows the approximate reconstruction of a side-layer solution.

Aleksandrova [5] applied the inertia-less core approximation to the problem of buoyant convection in a closed cavity with electrically insulating walls. The complete solution was obtained by matching separate solutions of the flow in the core, in the Hartmann layers, and in the side layers. The asymptotic relation (3) was used for the Hartmann layers, while the solution in the side layers was obtained by numerical integration.

Tagawa et al. [6] used a traditional finite-difference scheme for three-dimensional simulations of buoyant convection in a rectangular geometry. The asymptotic relation (3) accounted for friction and currents in the Hartmann layers, while the side layers were numerically resolved.

Leboucher [7] proposed a monotonically stable finite-difference scheme, with a fully staggered arrangement of velocity, pressure and electric potential. The algorithm was used for three-dimensional time-dependent simulations of unstable duct flows. As other authors, he applied the asymptotic relation (3) and the current sheet approximation for the Hartmann layers, but resolved the side layers numerically. Leboucher's stability analysis can be used in modified form to examine the stability properties of the collocated variable arrangement used in the present paper.

In this paper we propose a more general wall treatment for numerical simulations. Wall functions for velocity and electric potential are obtained by analytic integration of the steady-state governing equations, making use only of the local numerical solution. No assumptions are made regarding the orientation of the magnetic field relative to the wall, nor of the magnitude of the Hartmann number, or the wall conductivity. The wall functions are used in the specification of wall boundary conditions, but also for calculation of mass flow and electric currents in the near-wall cells. For demonstration and validation purposes the wall functions were implemented in a simple two-dimensional finite-volume algorithm. The wall function procedure as such is independent of the underlying discretization scheme, and should be easy to implement in most commercial flow solvers.

The wall function equations are derived in Section 2. In Section 3, numerical predictions are compared with an analytic solution for the case of fully developed duct flow in a transverse magnetic field. Details of the wall function treatment and its numerical implementation are summarized in Appendix A. The analytic solution used for validation is outlined in Appendix B.

2. Theory

2.1. Governing equations

With spatial coordinates **x** and time t, the Navier–Stokes and continuity equations for the velocity field $U_i(\mathbf{x},t)$ of an incompressible and electrically conducting fluid are

$$\frac{\partial \rho U_i}{\partial t} + U_j \frac{\partial \rho U_i}{\partial x_j} = -\frac{\partial P}{\partial x_i} + \frac{\partial}{\partial x_j}\left(\mu \frac{\partial U_i}{\partial x_j}\right) + \epsilon_{ikl} J_k B_l, \tag{4}$$

$$\frac{\partial U_i}{\partial x_i} = 0, \tag{5}$$

where $P(\mathbf{x},t)$ is the pressure field, ρ is fluid density, μ the fluid dynamic viscosity, and ϵ_{ikl} the alternating permutation tensor.

The last term in (4) is the magnetic Lorentz force, governed by the Maxwell equations. Here $B_i(\mathbf{x},t)$ is the magnetic flux density, and the electric current density $J_i(\mathbf{x},t)$ is given by Ohm's law,

$$J_i = \sigma\left(-\frac{\partial \Phi}{\partial x_i} + \epsilon_{ikl} U_k B_l\right), \tag{6}$$

where σ is the electric conductivity of the fluid, and Φ is the electric potential. In the absence of free charges, the electric current density is divergence free, $\nabla \cdot \mathbf{J} = 0$. If the electric conductivity is uniform, the divergence of (6) yields

$$\frac{\partial^2 \Phi}{\partial x_i \partial x_i} = \epsilon_{ijk} \frac{\partial}{\partial x_i}(U_j B_k). \tag{7}$$

If the characteristic length and velocity scales of the flow are h and v_0, respectively, the magnetic Reynolds number is defined as

$$R_m \equiv \mu_e \sigma v_0 h, \tag{8}$$

where μ_e is here the magnetic permeability. In the following we will assume that $R_m \ll 1$. This allows the use of the inductionless approximation, in which any distortion of the magnetic field by the fluid flow is assumed to be negligible. As a consequence, the magnetic flux density **B** in (4), (6) and (7) is given by the external magnetic field.

2.2. Near-wall analysis

Apart from the momentum and pressure equations, we will assume that a numerical simulation solves an equation for the electric potential Φ in the whole domain. Gradients of pressure and electric potential are computed from the solution. Near-wall model expressions of velocity and electric potential can then be obtained by analytic integration of the momentum and potential equations.

We consider a steady and approximately parallel flow close to a wall boundary with unit normal vector **n**, pointing into the flow. Let n be a coordinate along this normal vector, such that $n = 0$ at the wall, and $n > 0$ in the boundary layer. The velocity can be decomposed into components normal (n) and parallel (p) to the wall,

$$\mathbf{U} = \mathbf{U}_n + \mathbf{U}_p, \tag{9}$$

where

$$\mathbf{U}_n \equiv (\mathbf{U}\cdot\mathbf{n})\mathbf{n} = U_n\,\mathbf{n}, \tag{10}$$

$$\mathbf{U}_p \equiv \mathbf{U} - (\mathbf{U}\cdot\mathbf{n})\mathbf{n}. \tag{11}$$

We decompose the current density and the magnetic field in the same way,

$$\mathbf{J} \equiv \mathbf{J}_n + \mathbf{J}_p = J_n\,\mathbf{n} + (\mathbf{J} - J_n\,\mathbf{n}), \quad J_n \equiv \mathbf{J}\cdot\mathbf{n}, \tag{12}$$

$$\mathbf{B} \equiv \mathbf{B}_n + \mathbf{B}_p = B_n\,\mathbf{n} + (\mathbf{B} - B_n\,\mathbf{n}), \quad B_n \equiv \mathbf{B}\cdot\mathbf{n}. \tag{13}$$

In an arbitrary Cartesian coordinate system, we look at the momentum equation for the velocity parallel with the boundary, $\mathbf{U}_p$, and use the superscript i to identify its Cartesian components. If we neglect diffusion parallel with the walls as well as convection terms, and apply the decomposition above, Eq. (4) reduces to

$$\frac{\partial}{\partial n}\left(\mu \frac{\partial U_p^i}{\partial n}\right) = C^i - (\mathbf{J}_n \times \mathbf{B}_p)^i - (\mathbf{J}_p \times \mathbf{B}_n)^i, \tag{14}$$

where

$$C^i \equiv \big(\nabla P - \mathbf{n}(\nabla P \cdot \mathbf{n})\big)^i \tag{15}$$

is the i-th component of the wall-parallel part of the pressure gradient. Near the wall, C^i can be assumed independent of wall distance.

Excluding convective terms from (14) is consistent with the assumption that we are sufficiently close to the boundary for the flow to be approximately parallel ($U_n \ll U_p$). In the author's opinion, this is a necessary requirement in the region where boundary conditions are applied; if convective effects were to be significant here, they could hardly be fully accounted for by including the convective terms, in simplified form, in the integration of (14).

In (14), $\mathbf{J}_p \times \mathbf{B}_n$ is the term traditionally associated with a Hartmann layer, while $\mathbf{J}_n \times \mathbf{B}_p$ is the Lorentz force found in a parallel layer. It follows from the definitions (12) and (13) that $\mathbf{J}_n \times \mathbf{B}_n \equiv 0$. Note that generally $\mathbf{J}_p \times \mathbf{B}_p \neq 0$; $\mathbf{J}_p$ and $\mathbf{B}_p$ lie in the same plane, but are not necessarily parallel. Their vector product is however always normal to the wall, and does not contribute to (14).

In order to obtain an expression for the velocity profile in the boundary layer, we have to write the two Lorentz force terms in a form which allows (14) to be integrated.

2.2.1. *Hartmann layer term*

Using (6) and the decompositions above, we find for the Hartmann layer term

$$(\mathbf{J}_p \times \mathbf{B}_n)^i = -\sigma B_n(\nabla\Phi \times \mathbf{n})^i - \sigma B_n^2 U_p^i(n) + \sigma B_n U_n(n) B_p^i. \tag{16}$$

If the wall is insulating, the electric potential gradient parallel with the wall, $\nabla\Phi \times \mathbf{n}$, can be assumed constant during integration of (16) [2]. This holds approximately true also in the corner region, although current is injected into the Hartmann layer from the side layer. The assumption of constant $\nabla\Phi \times \mathbf{n}$ is accurate as long as the density of current *injected* into the Hartmann layer is negligible compared with the density of current transported in the Hartmann layer (driven by $\nabla\Phi$).

If the Hartmann wall is conducting, the current is transported in the wall itself, rather than in the boundary layer. In passing through the boundary layer, electric currents injected from the core and the side layers will cause the electric potential to change linearly with wall distance, due to Ohm's law. If the injected current varies along the wall, we must expect also the tangential potential gradient $\nabla\Phi \times \mathbf{n}$ to vary linearly with wall distance. For the integration of (16) we will therefor adopt the following general linearization of the tangential potential gradient term:

$$E^i \equiv \sigma B_n(\nabla\Phi \times \mathbf{n})^i = E_0^i + nE_1^i. \tag{17}$$

The second term in (16) contains U_p^i itself, and can be integrated as it is. The third term is proportional to the wall-normal velocity component U_n, rather than the wall-parallel velocity. Generally $U_n \ll U_p$, and near the wall $U_n \sim \mathrm{O}(n^2)$, while $U_p \sim \mathrm{O}(n)$. The third term is therefor small in comparison with other terms in (14), and will be neglected in the following.

2.2.2. *Parallel layer term*

The Lorentz force term acting in a parallel layer can be written

$$(\mathbf{J}_n \times \mathbf{B}_p)^i = -J_n(n) D_B^i, \tag{18}$$

where

$$D_B^i \equiv (\mathbf{B} \times \mathbf{n})^i. \tag{19}$$

In the case of insulating walls, $J_n = 0$ at the walls, and must remain small in the vicinity of the wall. This explains why (18) is very quickly dominated by the Hartmann terms in (16), unless $B_n = 0$, or at least $B_n \ll B_p$.

In order to integrate (18), we need to find an expression for the profile of $J_n(n)$ in the boundary layer. From (6) we can find

$$J_n = -\sigma\frac{\partial\Phi}{\partial n} + \sigma\mathbf{n} \cdot (\mathbf{U}_p \times \mathbf{B}_p), \tag{20}$$

but this only illustrates that J_n is the small difference between two large terms on the right-hand side, both of which will vary rapidly in the near-wall region. Instead we look at the electric potential equation (7), which can be written

$$\frac{\partial^2\Phi}{\partial n^2} + \nabla_p^2\Phi = \mathbf{n} \cdot \frac{\partial}{\partial n}(\mathbf{U}_p \times \mathbf{B}_p) + \nabla_p \cdot (\mathbf{U}_p \times \mathbf{B}_n) + \nabla_p \cdot (\mathbf{U}_n \times \mathbf{B}_p), \tag{21}$$

with the wall-parallel gradient operator

$$\nabla_p \equiv \nabla - \mathbf{n}\frac{\partial}{\partial n}. \tag{22}$$

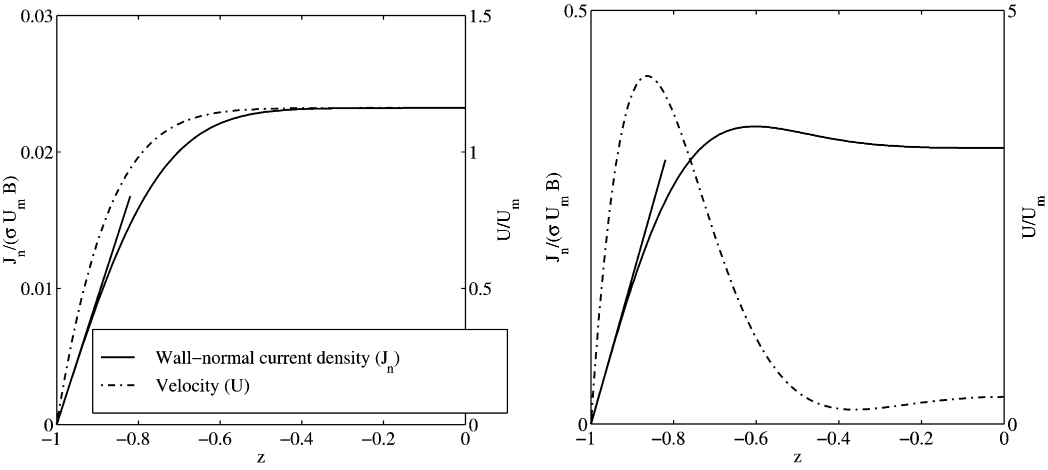

Fig. 1. Profiles of wall-normal current density (solid line) and velocity (dash-dotted line) in the center plane of a parallel layer (analytic solution in Appendix B; Ha = 50, $y = 0$). In the left figure, all walls are insulating. In the right figure, the side walls are insulating, but the Hartmann walls are perfectly conducting. The thin solid line shows a linear approximation of current density, using the true gradient at the wall.

The two last terms in (21) can be neglected, not only because gradients parallel with the boundary should be smaller than a gradient in the normal direction; we also note that $U_n \ll U_p$ (last term), and that the parallel layer term can be significant only if $B_n \ll B_p$. Recognizing the normal derivative of (20) allows us to write

$$\frac{\partial J_n}{\partial n} \approx \sigma \nabla_p^2 \Phi. \tag{23}$$

The variation of the wall-normal current in the boundary layer is thus related to the "wall-parallel Laplacian" (∇_p^2) of the electric potential. This suggests that the near-wall profile of J_n can be expected to be more regular than the profile of individual terms in (20).

To illustrate the situation, consider a fully developed flow in a square duct (this is the model problem treated in Section 3). The flow is in the x direction, with a transverse magnetic field in the y direction. The duct walls are located at $y = \pm 1$ and $z = \pm 1$; the former will develop Hartmann boundary layers, and the latter parallel boundary layers. For this case there are analytic solutions for the velocity and current densities, as described, e.g., by Müller and Bühler [8] (see Appendix B). Fig. 1 shows the profiles of velocity and wall-normal current density in the center plane of a parallel layer for Ha = 50, according to the analytic solution. In the left figure, all walls are insulating. In the right figure, side walls are insulating, but the Hartmann walls are perfectly conducting. In the latter case, the current density in the core is much higher, and most of the mass flow is concentrated in wall jets in the parallel layers.

Although the velocity profile and core current density is very different in the two cases, the profile of wall-normal current density in the boundary layer does not change much. Sufficiently close to the wall the profile of the wall-normal current density is approximately linear. It appears that even a rather moderate grid resolution would place the first computational node close enough to the wall for a linear approximation of $J_n(n)$ to be acceptable in a wall function.

In the following we assume that an estimate d_J for the gradient of the wall-normal current density can be computed from the numerical solution, and that the current J_{wall} into the wall is known (or given by the solution). For integration of (18), we can then take

$$J_n(n) = J_{\text{wall}} + n d_J. \tag{24}$$

2.2.3. *Wall function equations*

With (16)–(18) and (24), we can now write (14) as

$$\frac{\partial}{\partial n}\left(\mu \frac{\partial U_p^i}{\partial n}\right) = C^i + D_B^i (J_{\text{wall}} + n\, d_J) + E_0^i + n\, E_1^i + \sigma B_n^2 U_p^i. \tag{25}$$

If the wall shear stress is $\tau^i = \mu(\partial U_p^i/\partial n)(0)$ (*a priori* unknown), and with zero velocity ("no-slip") at the wall, Eq. (25) can be integrated to give an expression for the wall-parallel component of the velocity in the boundary layer,

$$U_p^i(n) = \tau^i \frac{\delta_H \sinh(n/\delta_H)}{\mu} + \left(C^i + J_{\text{wall}} D_B^i + E_0^i\right) \frac{\delta_H^2}{\mu}\left(\cosh\left(\frac{n}{\delta_H}\right) - 1\right)$$

$$+\left(d_J D_B^i + E_1^i\right)\frac{\delta_H^3}{\mu}\left(\sinh\left(\frac{n}{\delta_H}\right) - \frac{n}{\delta_H}\right), \tag{26}$$

where δ_H is a local Hartmann length scale defined in terms of the wall-normal component of the magnetic field,

$$\delta_H \equiv \frac{1}{|B_n|}\sqrt{\frac{\mu}{\sigma}}. \tag{27}$$

This local definition means that $1/\delta_H = 0$ in a parallel layer, where $B_n = 0$. For this case, and when $B = 0$, Eq. (26) has a limit value. For small B_n one can instead use a series expansion about $1/\delta_H = 0$ (see Appendix A).

Eq. (26) can be used for defining implicit velocity boundary conditions in a numerical simulation; see Appendix A for details. For completeness, the formulation of the velocity wall function equations in Appendix A also allows for a non-zero tangential wall velocity; although not exploited in the present paper, this could be of interest to colleagues dealing with free-surface flows.

Eq. (26) can be integrated to yield an expression for the average parallel velocity in the near-wall region,

$$\overline{U}_p^i(n) \equiv \frac{1}{n}\int_0^n U_p^i(n')\,\mathrm{d}n'. \tag{28}$$

In order to accurately predict the current production in the unresolved near-wall region of a numerical simulation, the average velocity should be used for computing the source term in the electric potential equation, as well as for computing the total current density and the Lorentz force.

The near-wall profile of the electric potential can be derived from (20), which is first rewritten as

$$\frac{\partial \Phi}{\partial n} = -\frac{1}{\sigma}J_n(n) + (\mathbf{U}_p \times \mathbf{B}_p)\cdot\mathbf{n} = -\frac{1}{\sigma}J_n(n) + (\mathbf{B}\times\mathbf{n})\cdot\mathbf{U}_p. \tag{29}$$

We integrate this expression, assuming **B** is constant over integration, and using the linear model (24) of the wall-normal current density. With the definition (28) of average parallel velocity $\overline{\mathbf{U}}_p$, the result can be written

$$\Phi(n) = \Phi_{\text{wall}} - \frac{nJ_{\text{wall}}}{\sigma} - \frac{n^2 d_J}{2\sigma} + (\mathbf{B}\times\mathbf{n})\cdot\overline{\mathbf{U}}_p(n), \tag{30}$$

where $\Phi_{\text{wall}} = \Phi(0)$ is the electric potential at the wall. This expression can be used to compute *a posteriori* the electric potential at an insulating boundary, or to define implicit boundary conditions in the case of a conducting boundary.

3. Numerical predictions

For demonstration purposes, the wall functions derived in Section 2.2 have been used for numerical simulation of a fully developed flow in a square channel, with channel half-width h and cross-section area $A = 4h^2$. The coordinate system is chosen so that the flow is in the x direction, with a transverse magnetic field in the y direction; see Fig. 2. The duct walls are located at $y = \pm h$ and $z = \pm h$; the former will develop Hartmann boundary layers, and the latter parallel boundary layers. Numerically predicted pressure drop and wall friction coefficients were compared with analytic solutions available for this geometry. The analytic solutions are described in Appendix B.

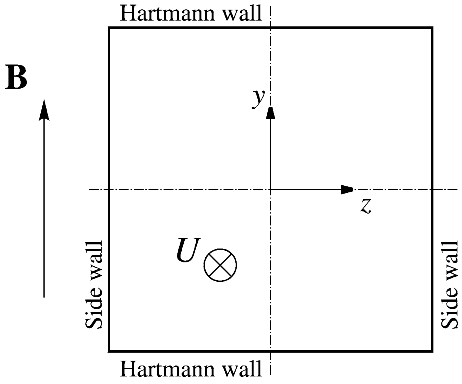

Fig. 2. Square duct geometry and coordinates.

The flow solver uses finite volume discretization with collocated primary variables U and Φ stored in cell centers. The grid is orthogonal, but not necessarily uniform. Electric currents and source terms for the electric potential equation are consistently computed on cell faces to guarantee conservation of electrical current. The current density contributions $-\sigma\nabla\Phi$ and $\sigma\mathbf{U}\times\mathbf{B}$ in cell centers are computed separately as averages of facial values. See Appendix A for details on the finite volume representation of the proposed wall functions.

To improve the convergence for large Hartmann numbers, the velocity and electric potential equations are solved simultaneously, with the source terms in the bulk defined implicitly in both equations. Inter-variable references in the wall boundary conditions are however still defined explicitly and iterated. The use of the cell average velocity for computing $\mathbf{U}\times\mathbf{B}$ on the faces of near-wall cells also gives rise to an explicit correction of the source terms in both velocity and potential equations.

We define Reynolds and Hartmann numbers as

$$\mathrm{Re}\equiv\frac{\rho U_m h}{\mu}, \tag{31}$$

$$\mathrm{Ha}\equiv\sqrt{\frac{\sigma}{\mu}}Bh, \tag{32}$$

where U_m is the mean velocity in the cross-section. All calculations below are for $\mathrm{Re}=100$.

In the simulations, the constant pressure gradient $C=\mathrm{d}P/\mathrm{d}x$ is adjusted to obtain a desired mean velocity U_m, or massflow $Q=\rho AU_m$. The net Lorentz force (per unit length) over the cross-section area A is

$$F_L=\int_A(\mathbf{J}\times\mathbf{B})\cdot\mathrm{d}\mathbf{A}, \tag{33}$$

and the contribution of the Lorentz force to the total pressure drop is thus $F_L/(CA)$. The total wall friction can be expressed in terms of a non-dimensional friction coefficient,

$$c_f\equiv\frac{|\tau_m|}{\rho U_m^2/2}=\frac{|-CA-F_L|/(8h)}{\rho U_m^2/2}, \tag{34}$$

where τ_m is the mean wall shear stress along the perimeter $(8h)$ of the channel.

3.1. Insulating walls

In the case of insulating walls, the electric currents close in the flow domain. This means there is no net Lorentz force in a cross section ($F_L=0$), and the wall friction alone is responsible for the pressure drop.

Table 1 shows numerically predicted friction coefficients obtained with the new wall functions, compared with the coefficients obtained with conventional linear interpolation to the wall. The grid is uniform, 20 × 20. The numerical predictions c_f^{num} are shown relative to the values c_f^{an} obtained from the analytic solution (see Appendix B). With conventional linear interpolation to the wall, the predicted wall shear stress deteriorates with increasing Hartmann numbers. With the proposed wall functions the result is typically within 1–1.6% of the analytical values. The reason the error is largest $(+1.6\%)$ for $\mathrm{Ha}=30$ is the linear discretization between the first and second nodes (the first node is in the Hartmann layer, the second in the core). The wall function prediction is better than the linear interpolation also for $\mathrm{Ha}=0$, because the series expansion of the velocity wall function contains also a quadratic term proportional to the pressure gradient.

Fig. 3 shows how the accuracy of the predicted friction coefficient depends on near-wall grid resolution of the Hartmann layer. The thickness of the Hartmann layer is proportional to the Hartmann distance $\delta_H=h/\mathrm{Ha}$, which is used here to scale the near-wall grid size Δy. Without wall functions (left), the relative error of the friction coefficient increase with grid size. With the proposed wall function in the Hartmann layer (right), the accuracy is virtually insensitive to grid resolution. Without wall functions at least 5–6 grid cells are required inside the Hartmann layer to obtain a comparable accuracy.

Assuming the wall function treatment is applied at Hartmann walls, Fig. 4 shows the benefit of using the wall functions also for the side layers. Either way, the accuracy depends on the resolution of the boundary layers at the side walls. Without wall functions, however, the grid resolution must be doubled to obtain the same accuracy as with the wall functions. With the same grid, the wall function treatment reduces the error by a factor of two.

The two graphs in Fig. 5 show predicted local wall shear stresses along Hartmann and side walls, respectively, in comparison with the analytic solution ($\mathrm{Ha}=100$, uniform grid 20 × 20). The wall functions allow very accurate prediction of the local wall shear stress, even with on this coarse grid. The error is highest for corner cells (far left in the second graph), which have one face at a Hartmann wall, and one at a side wall. This error diminishes rapidly if the resolution of the side layer is improved, and the error is too small to justify any special treatment of the corner region.

Table 1
Numerically predicted friction coefficients c_f^{num}, relative to values c_f^{an} obtained from the analytic solution (see Appendix B), for a number of different Hartmann numbers. The grid is uniform, 20 × 20. The left column is for conventional linear interpolation to the walls, while values in the right column are obtained with the analytic wall function

Ha	Friction coefficient, $c_f^{\text{num}}/c_f^{\text{an}}$	
	Linear interp.	Wall functions
0	0.990	1.000
10	0.905	1.011
30	0.596	1.016
100	0.228	0.995

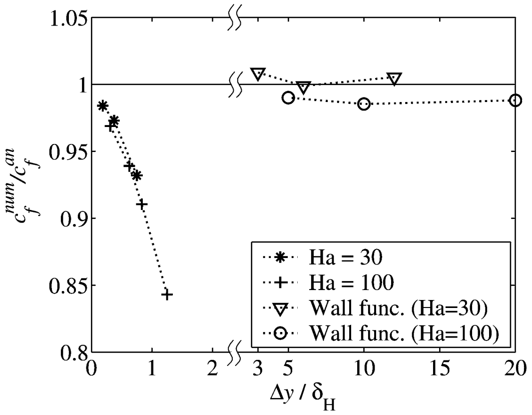

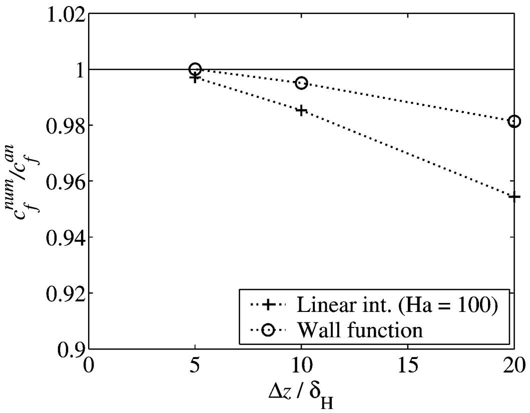

Fig. 3. The graph shows how the near-wall grid size in the Hartmann layers affect the accuracy of predicted friction coefficients. The near-wall grid size Δy is scaled by the Hartmann distance $\delta_H = h/\text{Ha}$. Note the broken horizontal axis. Results on the left are without wall functions, using local grid refinement to resolve the Hartmann layers. The results on the right were obtained with the proposed wall functions applied in the Hartmann layer (but not in the side layers). All calculations used 20 grid cells in the z-direction ($\Delta z/\delta_H = 10$).

Fig. 4. Accuracy of predicted friction coefficients, versus near-wall grid size in the parallel layers (Ha = 100). Near-wall grid size Δz is scaled by the Hartmann distance $\delta_H = h/\text{Ha}$. Results are obtained with standard linear interpolation and with wall functions, respectively, at the side walls. In both cases wall functions were applied at the Hartmann walls (20 cells in y direction, $\Delta y/\delta_H = 10$).

Fig. 6 shows the U velocity profile (left) and the profile of wall-normal current density J_z in the side layer for $\text{Ha} = 100$ (center of channel, $y = 0$). Both velocity and current density are accurately predicted with the wall functions. The short-comings of standard linear interpolation are seen here as a very different velocity profile (the mean velocity is fixed), and a dramatic under-prediction of current density in the core.

Application of the wall function for electric potential gives only a rather small improvement of accuracy (typically 0.2% for a final accuracy of the pressure drop in the range 0.3 to 1.6%). It may however be convenient for defining implicit boundary conditions in the case of finite wall conductivities, where the electric solution in the flow must be matched to a solution for the currents in the walls.

3.2. Conducting Hartmann walls

In this case currents generated by the flow can close in the Hartmann walls, rather than in the Hartmann boundary layers. The total pressure drop is dominated by the Lorentz force, and the flow is characterized by wall jets in the side layers, which carry a large part of the mass flow. The current is generated mainly in the wall jets, and the accuracy of the pressure drop prediction thus depends on the resolution of the wall jet.

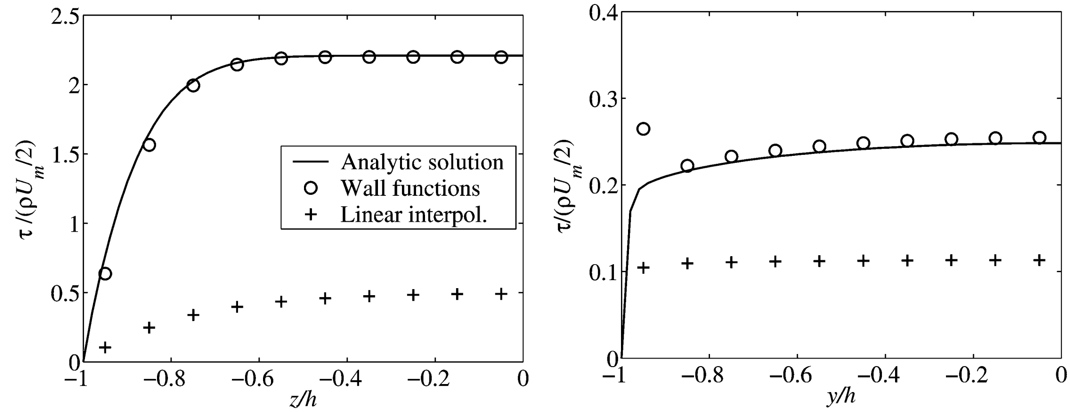

Fig. 5. Numerically predicted local wall shear stress along Hartmann walls (left) and side walls (right) for Ha = 100, obtained with wall functions (o), and with standard linear interpolation (+). The solid lines represent the analytic solution. The wall shear stress is scaled by the dynamic pressure $\rho U_m^2/2$.

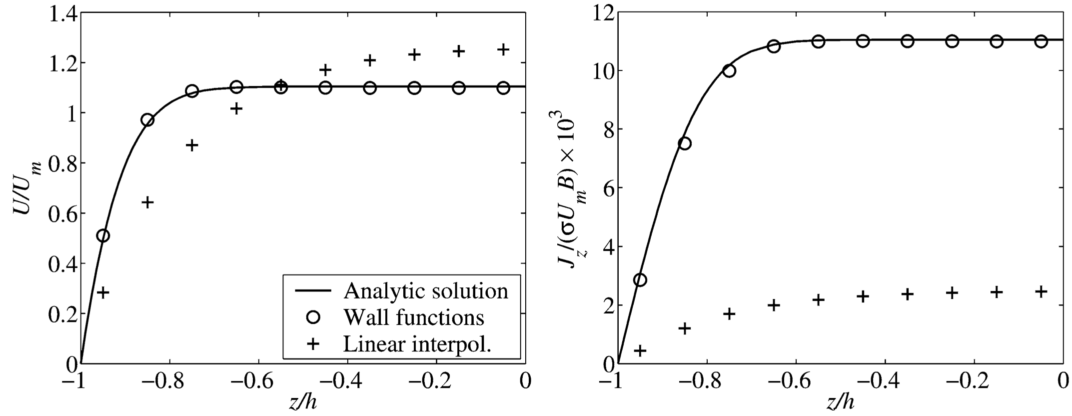

Fig. 6. Center-line velocity (left) and current density (right) profiles in the side layer for Ha = 100 ($y = 0$), as predicted with wall functions and with linear interpolation, respectively (uniform grid 20 × 20). Solid lines show the analytic solution.

Table 2
Numerically predicted pressure drops, Lorentz forces, and friction coefficients c_f^{num}, relative to values obtained from the analytic solution. The second column shows the contribution of the Lorentz force to the total pressure drop. The grids were chosen to resolve the wall jets in the side layers with 10–12 cells. In the first two cases the grid was uniform; 20 × 20 for Ha = 10, and 20 × 30 for Ha = 30. For Ha = 100, the 20 × 20 grid was refined by a factor two in the z direction near the wall (corresponding to a 20 × 40 grid in the region of the wall jets)

Ha	$\left(\frac{F_L}{-AC}\right)^{\mathrm{an}}$ (%)	Linear interp.			Wall functions		
		$\frac{C^{\mathrm{num}}}{C^{\mathrm{an}}}$	$\frac{F_L^{\mathrm{num}}}{F_L^{\mathrm{an}}}$	$\frac{c_f^{\mathrm{num}}}{c_f^{\mathrm{an}}}$	$\frac{C^{\mathrm{num}}}{C^{\mathrm{an}}}$	$\frac{F_L^{\mathrm{num}}}{F_L^{\mathrm{an}}}$	$\frac{c_f^{\mathrm{num}}}{c_f^{\mathrm{an}}}$
10	71	0.972	0.985	0.938	0.997	0.992	1.010
30	87	0.963	0.980	0.855	0.996	0.994	1.014
100	93	0.966	0.975	0.837	0.994	0.993	1.007

Table 2 shows numerically predicted pressure drops, Lorentz forces and friction coefficients. The wall function calculation of average velocity in the near-wall cells significantly improves the prediction of mass flow and current generation in the side layers, and the wall functions remain essential for a correct prediction of wall friction.

Similar to the case with isolating walls, the solution is rather independent of the resolution of the Hartmann layer. For the parallel layers, Fig. 7 suggests that the improvement of accuracy obtained with the wall functions is at least as important as for the insulating case.

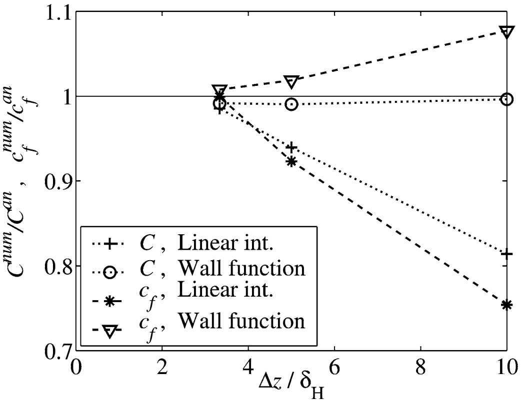

Fig. 7. Accuracy of predicted pressure drops and friction coefficients, versus near-wall grid size in the parallel layers (Ha = 100). Results were obtained with standard linear interpolation and with wall functions, respectively, at the side walls. In both cases wall functions were applied at the Hartmann walls (20 cells in y direction, $\Delta y/\delta_H = 10$).

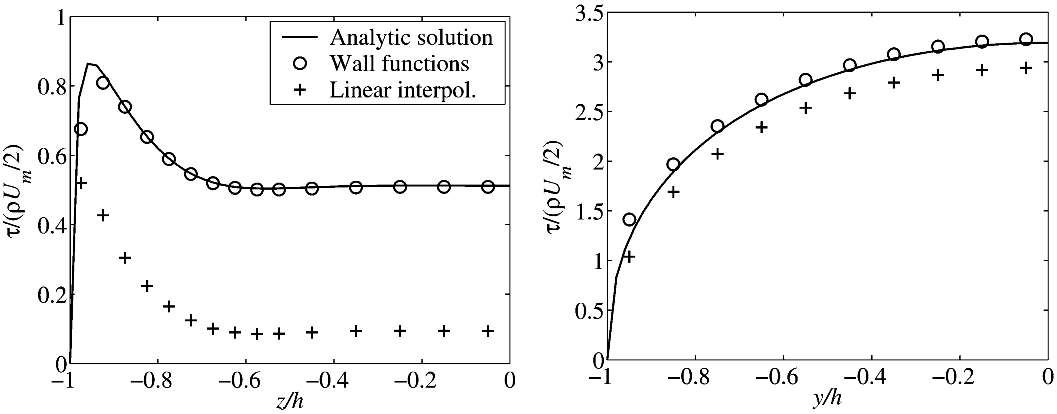

Fig. 8. Numerically predicted local wall shear stresses along Hartmann walls (left) and side walls (right), in case of perfectly conducting Hartmann walls and Ha = 100. Results were obtained with wall functions (o), and with standard linear interpolation (+), respectively. The solid lines represent the analytic solution. The wall shear stress is scaled by the dynamic pressure $\rho U_m^2/2$.

Due to the wall jets, the wall friction is larger in the side layers than in the Hartmann layers, as shown in Fig. 8. The effect of the wall functions is however still strongest for the Hartmann layers.

Fig. 9 shows the velocity profile (left) and the profile of wall-normal current density in the side layer for Ha = 100 ($y = 0$). Since the flow resistance is dominated by the bulk Lorentz force, the effect of the wall boundary conditions on the bulk velocity and current distributions is not as striking as in the case of insulating walls.

Leboucher [7] computed the same case using the high-Ha exponential profile (3) for modeling of the Hartmann boundary layer. For the case Ha = 100 and uniform grids $N_y \times N_z = 8 \times 32,\ 16 \times 64$ and 32×128, Leboucher reports prediction accuracies of 7%, 2% and 0.3%, respectively. With the wall function treatment proposed in the present paper, the accuracy of pressure drop predictions is 0.4% already on the coarsest grid (8 × 32).

The stability analysis of Leboucher [7] showed that the numerical stability of a standard staggered arrangement of variables depend on the grid resolution perpendicular to the magnetic field. The corresponding condition for monotonic stability was found to be $\Delta z/\delta_H \leqslant 2\sqrt{2}$. The criterion for stability thus varies as Ha^{-1}, although the thickness of the parallel boundary layer varies only as $\mathrm{Ha}^{-1/2}$. Leboucher's analysis can easily be modified for the collocated variable arrangement used in this paper, which yields the condition $\Delta z/\delta_H \leqslant 2$. In this paper (as well as in Leboucher's) there are signs of instability only in the case of conducting Hartmann walls: the case of Ha = 100 and a uniform grid 20 × 20 was stable when the wall functions were used, but showed weak oscillations near the corners with standard linear interpolation. For this case $\Delta z/\delta_H = 10$, which is five times higher than the formal monotonic stability criterion.

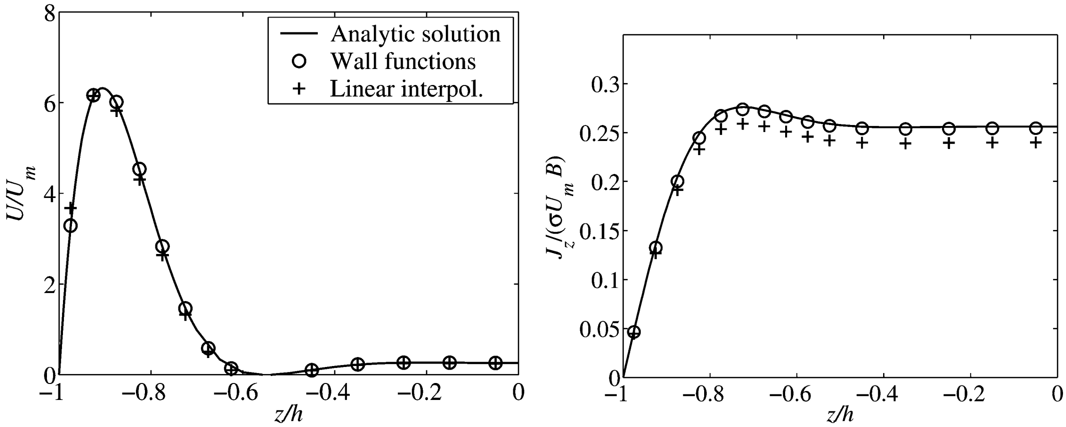

Fig. 9. Center-line velocity (left) and current density (right) profiles in the side layer ($y = 0$), for perfectly conducting Hartmann walls and Ha = 100. Results obtained with wall functions (o) and linear interpolation (+), respectively. Solid lines show the analytic solution.

4. Summary and conclusions

In this paper a general wall function treatment is proposed for numerical modeling of laminar MHD flows. The wall function expressions are derived analytically from the momentum and electric potential equations, making use only of the local numerical solution. The derivation is simplified by the decomposition of vectorial quantities into components parallel and normal to the wall boundary. No assumptions are made regarding the orientation of the magnetic field relative to the wall, nor of the magnitude of the Hartmann number, or the wall conductivity.

The velocity wall function is used not only for defining the velocity boundary condition, but also for accurately computing $\mathbf{U} \times \mathbf{B}$ on the faces of near-wall cells. This is essential for an accurate calculation of the Lorentz force and the source term in the electric potential equation.

The wall function treatment has been validated in a simple two-dimensional finite volume formulation. The test case is a fully developed duct flow in a transverse magnetic field, with insulating parallel walls, and Hartmann walls either insulating or perfectly conducting. For this case numerical predictions could be compared with an analytic solution.

With the wall functions, the accuracy of predicted pressure drop and wall shear stress becomes essentially independent of the resolution of the Hartmann layers. When applied also to the parallel layers, the errors are reduced by a factor two to three. With a conventional treatment of the parallel walls, the grid resolution of the parallel layers would have to be doubled or tripled to obtain a comparable accuracy. For the case of insulating walls and Hartmann numbers from 0 to 100, a uniform grid $N_y \times N_z = 20 \times 20$ gives an accuracy of pressure drop and wall shear stress predictions within 1.6% of the analytic solution. Similar results are obtained for the case of conducting Hartmann walls, as long as there is reasonable resolution of the wall jets in the parallel layers (N_z up to 40 for Ha = 100).

The wall function for electric potential (Eq. (30)) proposed in this paper offers only a rather small improvement of accuracy (typically 0.2%, for a final accuracy of the pressure drop in the range 0.3 to 1.6%). It may however be convenient for defining implicit boundary conditions in the case of finite wall conductivities, and matching to a solution for the currents in the walls.

The results shown here are for a simple geometry, for which analytic solutions can be used for validation. The treatment has recently been successfully implemented in an in-house MHD module for a commercial flow solver. This will allow extensive tests to be made also for more demanding configurations.

The wall treatment presented in this paper is different from other methods described in the literature, in that the derivation is equally valid for all values of the Hartmann number, and in that it considers also the effects present in parallel layers. The formulation is strictly local, and independent of the direction of the magnetic field. The wall functions can be easily implemented in any general flow solver, to allow accurate predictions at reasonable cost also in complex geometries and nonuniform magnetic fields.

Acknowledgement

The author gratefully acknowledges the support provided by a Marie Curie Fellowship of the European Community programme “Human Potential”, under contract number HPMFCT-2000-00585.

Appendix A. Summary of wall function equations

A.1. Velocity

The local Hartmann length scale is defined in terms of the wall-normal component B_n of the magnetic field,

$$\delta_H \equiv \frac{1}{|B_n|}\sqrt{\frac{\mu}{\sigma}}. \tag{35}$$

For practical reasons, we define also the inverse of δ_H,

$$k_H \equiv \frac{1}{\delta_H}. \tag{36}$$

The wall-normal current density is assumed to vary linearly with gradient d_J in the unresolved near-wall region. If J_{wall} is the current density through the wall, and $J_n(n_P)$ is the wall-normal current density in the first computational node n_P in the flow (as given by the solution), the gradient is estimated as

$$d_J = \frac{J_n(n_P) - J_{\text{wall}}}{n_P}. \tag{37}$$

Let $\mathbf{n}$ be a unit vector normal to the wall (pointing into the flow), and define

$$C^i \equiv \big(\nabla P - \mathbf{n}(\nabla P \cdot \mathbf{n})\big)^i, \tag{38}$$

$$D_B^i \equiv (\mathbf{B} \times \mathbf{n})^i, \tag{39}$$

where the magnetic field and the pressure gradient are taken in the first computational node. Further assume that the near-wall variation of the electric potential gradient can be linearized such that

$$E^i \equiv \sigma B_n (\nabla \Phi \times \mathbf{n})^i = E_0^i + n\, E_1^i. \tag{40}$$

The way J_{wall}, E_0^i and E_1^i above are determined depends on the electric properties of the wall. For an insulating wall $J_{\text{wall}} = 0$, and the wall-parallel gradient of electric potential is approximately constant. We can then write

$$E_0^i = E_P^i, \qquad E_1^i = 0, \tag{41}$$

where E_P^i is the value computed with the potential gradient in the first computational node $n = n_P$.

For a perfectly conducting wall, the electric potential has a constant value (and zero parallel gradient) at the wall, and we instead take

$$E_0^i = 0, \qquad E_1^i = \frac{E_P^i}{n_P}. \tag{42}$$

With zero velocity at the wall, the wall current can be calculated as $J_{\text{wall}} = -\sigma(\partial\Phi/\partial n)(0)$. (In this case Eq. (37) is likely to produce $d_J = 0$.)

For the general case of finite wall conductivity, we assume that the numerical solution in the fluid is somehow coupled to a solution of the electrical equations in the wall. The wall current J_{wall} should then be available as part of the coupling. E_0^i and E_1^i can be calculated from E_P^i and the parallel gradient of electric potential computed at the wall itself.

If τ^i and U_{wall}^i are the i-th Cartesian components of the wall shear stress and the tangential wall velocity, respectively, the components of velocity parallel with the wall is given in the near-wall region by

$$U_p^i\big(n, \tau^i, U_{\text{wall}}^i\big) = f_\tau(n)\tau^i + f_U(n)U_{\text{wall}}^i + f_C^i(n), \tag{43}$$

where

$$f_\tau(n) = \frac{\sinh(n\,k_H)}{\mu\, k_H}, \tag{44}$$

$$f_U(n) = \cosh(n\,k_H), \tag{45}$$

$$f_C^i(n) = \big(C^i + J_{\text{wall}} D_B^i + E_0^i\big)\frac{\cosh(n\,k_H) - 1}{\mu k_H^2} + \big(d_J D_B^i + E_1^i\big)\frac{\sinh(n\,k_H) - n\,k_H}{\mu k_H^3}. \tag{46}$$

The split into functions f_τ, f_U (scalars) and f_C^i (vector) is useful for defining implicit velocity boundary conditions (see Appendix A.3). Since the present paper considers only "no-slip" walls ($U_{\text{wall}}^i = 0$), the function f_U is never used. It is included here for completeness.

The wall shear stress can be computed from the obtained solution as

$$\tau^i = \frac{1}{f_\tau(n_P)}\big(U_p^i(n_P) - f_U(n_P)\,U_{\text{wall}}^i - f_C^i(n_P)\big), \tag{47}$$

where $U_p^i(n_P)$ is the predicted parallel velocity in the first computational node $n = n_P$.

The average velocity in a near-wall region $0 \leqslant n \leqslant n'$, such that $n' \leqslant n_P$, is computed by integration of (43),

$$\begin{aligned}\overline{U}_p^i(n') \;\equiv\; \frac{1}{n'}\int_0^{n'} U_p^i(n)\,\mathrm{d}n &= \tau^i\,\frac{\cosh(n'k_H)-1}{\mu n' k_H^2} + \big(C^i + J_{\text{wall}}D_B^i + E_0^i\big)\frac{\sinh(n'k_H) - n'k_H}{\mu n' k_H^3} \\ &\quad + \big(d_J D_B^i + E_1^i\big)\left(\frac{\cosh(n'k_H)-1}{\mu\, n'\, k_H^4} - \frac{n'}{2\mu\, k_H^2}\right) + U_{\text{wall}}^i\,\frac{\sinh(n'k_H)}{n'k_H}\end{aligned} \tag{48}$$

with τ^i given by (47). It is important not to extrapolate the integration beyond the point n_P used in (47), because the function (43) may produce unphysical values of U_p^i for $n > n_P$ (see Appendix A.3).

Eqs. (44), (46) and (48) have limit values when $k_H \to 0$, i.e., when $B_n \to 0$. For sufficiently small values of k_H one can instead use a series expansion about $k_H = 0$. As a local criterion for when this is applicable one can use

$$n_P\, k_H < \varepsilon, \quad \varepsilon \ll 1, \tag{49}$$

where n_P is the wall distance of the first computational node.

If all terms of order $(n\,k_H)^4$ and higher are truncated, we have

$$f_\tau(n) = \frac{n}{\mu} + \frac{n^3 k_H^2}{6\mu}, \tag{50}$$

$$f_U(n) = 1 + \frac{1}{2}n^2 k_H^2, \tag{51}$$

$$f_C^i(n) = \big(C^i + J_{\text{wall}}D_B^i + E_0^i\big)\left(\frac{n^2}{2\mu} + \frac{n^4 k_H^2}{24\mu}\right) + \big(d_J D_B^i + E_1^i\big)\left(\frac{n^3}{6\mu} + \frac{n^5 k_H^2}{120\mu}\right). \tag{52}$$

The truncated series expansion of the mean parallel velocity (48) is

$$\begin{aligned}\overline{U}_p^i(n') \;=\; &\tau^i\left(\frac{n'}{2\mu} + \frac{n'^3 k_H^2}{24\mu}\right) + \big(C^i + J_{\text{wall}}D_B^i + E_0^i\big)\left(\frac{n'^2}{6\mu} + \frac{n'^4 k_H^2}{120\mu}\right) \\ &+ \big(d_J D_B^i + E_1^i\big)\left(\frac{n'^3}{24\mu} + \frac{n'^5 k_H^2}{720\mu}\right) + U_{\text{wall}}^i\left(1 + \frac{1}{6}n'^2 k_H^2\right).\end{aligned} \tag{53}$$

A.2. Electric potential

The near-wall profile of electric potential is described by

$$\Phi(n) = \Phi_{\text{wall}} - \frac{n\,J_{\text{wall}}}{\sigma} - \frac{n^2 d_J}{2\sigma} + n\,(\mathbf{B}\times\mathbf{n})\cdot\overline{\mathbf{U}}_p(n), \tag{54}$$

where $\Phi_{\text{wall}} = \Phi(0)$ is the electric potential at the wall, and $\overline{\mathbf{U}}_p(n)$ is the mean parallel velocity (48).

How this expression is used in a numerical simulation depends on the electrical properties of the wall boundary. For insulating walls one can use a simple zero flux ($\partial\Phi/\partial n = 0$) boundary condition for the electric potential equation, and (54) could be used to compute Φ_{wall} from the obtained solution (i.e., $\Phi(n_P)$ and $\overline{\mathbf{U}}_p(n_P)$ in the first computational node).

For a perfectly conducting boundary the wall potential Φ_{wall} is supposed to be known, and (54) could be used to define an implicit boundary condition, in the same way as for the velocity (noting that $J_{\text{wall}} = (\partial\Phi/\partial n)_{\text{wall}}$ when $U_{\text{wall}} = 0$). This allows J_{wall} to be computed from the obtained solution.

For a boundary with finite conductivity the complete expression (54) can be used to match the solution in the flow with a solution in the wall itself.

A.3. Notes on implementation

For an example of how the wall functions can be implemented in a numerical solver, we assume here a steady-state finite volume discretization with collocated variables, so that both pressure, electrostatic potential, and velocity components are stored at cell centers. We further assume a grid such that the first control volume has its west face w at the wall and its center at P, as shown in Fig. 10. The area of the west face is A_w, and its normal vector is $\mathbf{n}$. We assume the solver solves a generic transport equation, which for a variable Q can be written on the form

$$\nabla \cdot (\rho \mathbf{U} Q - \Gamma\, \nabla Q) = S, \tag{55}$$

where Γ is the relevant effective diffusivity of the variable. The source term S is usually linearized as $S = S_p Q + S_u$. Integration over a control volume yields (using Gauss' law)

$$\int (\rho Q \mathbf{U} - \Gamma \nabla Q) \cdot \mathrm{d}\mathbf{A} = \int S \, \mathrm{d}V, \tag{56}$$

with d**A** pointing out of the control volume.

We apply (56) on the U momentum equation for a cell next to a no-slip wall with $\mathbf{n} = \mathbf{e}_y$, and wall distance y_P. The integral over the west face, with $\mathrm{d}\mathbf{A} = -\mathbf{e}_y A_w$, yields

$$\int\limits_{A_w} (\rho U \mathbf{U} - \mu \nabla U) \cdot \mathrm{d}\mathbf{A} = \left(\rho U(-V) + \mu \frac{\partial U}{\partial y} \right) A_w = \mu \frac{\partial U}{\partial y} A_w = A_w \tau_w. \tag{57}$$

But from (47) we have

$$\tau_w = \frac{1}{f_\tau(y_P)} \big(U_P(y_P) - f_C^{(x)}(y_P) \big), \tag{58}$$

so that

$$\int\limits_{A_w} (\rho U \mathbf{U} - \mu \nabla U) \cdot \mathrm{d}\mathbf{A} = \frac{A_w}{f_\tau(y_P)} \big(U_P(y_P) - f_C^{(x)}(y_P) \big). \tag{59}$$

This is implemented in the discretized equations by setting the corresponding matrix coefficient a_w of the face at the wall to zero, and modifying the source terms for the first near-wall cell,

$$a_w = 0, \tag{60}$$

$$S_p \leftarrow S_p - \frac{A_w}{f_\tau(y_P)}, \tag{61}$$

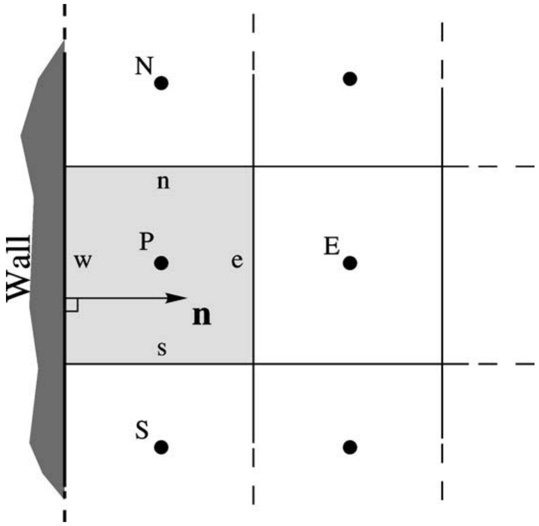

Fig. 10. Discretization of near-wall cells.

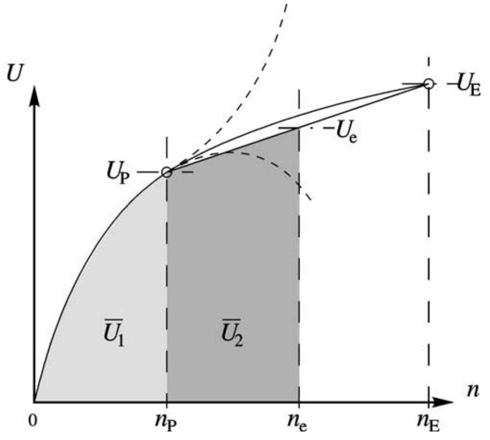

Fig. 11. Calculation of average parallel velocity in a near-wall cell.

$$S_u \leftarrow S_u + \frac{A_w f_C^{(x)}(y_P)}{f_\tau(y_P)}. \tag{62}$$

For an accurate calculation of the total current density and the electric potential source term in the near wall cells, it is important to use a cell average velocity computed with the wall function for calculation of $\mathbf{U} \times \mathbf{B}$ on the cell faces. Naively using the velocity stored in the cell center would overestimate $\mathbf{U} \times \mathbf{B}$. The calculation of cell average velocity in this paper is illustrated in Fig. 11. It is tempting to use the average velocity expression (48) integrated over the whole cell. The velocity wall function may however exhibit under- or overshoots beyond the cell center $n = n_P$. Instead we use (48) for the average $\overline{U}_1$ in the inner half of the cell, and a linear interpolation toward the neighboring cell opposite the wall boundary for the average $\overline{U}_2$ in the outer half of the cell. With the notation in Fig. 11, U_e is the parallel velocity at the east face ($n = n_e$), interpolated from the cell center values U_P and U_E. It is practical to treat the cell average velocity as proportional to U_P,

$$U_{\mathrm{av}} = f_{\mathrm{av}}\, U_P, \tag{63}$$

where

$$U_{\mathrm{av}} = \frac{\overline{U}_1 + \overline{U}_2}{2} = \frac{|\overline{U}_p^i(n_P)| + (U_P + U_e)/2}{2}. \tag{64}$$

For cells facing more than one wall boundary (presumably a corner), factors f_{av} have simply been multiplied in this paper. The factor f_{av} is set to unity immediately before a new iteration, and updated when velocity boundary conditions are set. When electric potential source terms and total currents are computed, Eq. (63) is used to compute the cell average velocity.

Appendix B. Analytic solution for rectangular channel flow

For fully developed flow in a rectangular channel with insulating or perfectly conducting walls, there exists analytic solutions which can be used for validation of the wall function predictions. We here use the solutions, as described by Müller and Bühler [8], for the case of insulating walls, and for the case where the Hartmann walls are perfectly conducting.

The flow is in the x direction, with streamwise velocity $u(y,z)\mathbf{e}_x$. The external magnetic field is in the y direction, and the problem is scaled so that the channel half-width h in this direction is unity ($h = 1$), with Hartmann walls located at $y = \pm 1$. The channel half-width perpendicular to the magnetic field is d, with side walls at $z = \pm d$. The velocity scale is

$$v_0 = \frac{h^2(-\partial P/\partial x)}{\mu}, \tag{65}$$

with which the magnitude of the uniform pressure gradient evaluates to unity. The external magnetic field is scaled with itself, and the total magnetic field is decomposed as

$$\mathbf{B} = \mathbf{e}_y + \frac{R_m}{\mathrm{Ha}}\mathbf{b}, \tag{66}$$

where the magnetic field induced by the flow, $\mathbf{b}$, is scaled by R_m/Ha. The only non-zero component of the induced field is in the x direction, so that $\mathbf{b} = b(y,z)\mathbf{e}_x$. The current density can then be written as

$$\mathbf{j} = \frac{1}{\mathrm{Ha}}\nabla \times b\mathbf{e}_x = \frac{1}{\mathrm{Ha}}\left(\frac{\partial b}{\partial z}\mathbf{e}_y - \frac{\partial b}{\partial y}\mathbf{e}_z\right). \tag{67}$$

The solution is obtained by expanding the velocity and the induced magnetic field into Fourier series,

$$u = \sum_{i=1,3,5}^{\infty} u_i(y)\cos(\lambda_i z), \tag{68}$$

$$b = \sum_{i=1,3,5}^{\infty} b_i(y)\cos(\lambda_i z), \tag{69}$$

with

$$\lambda_i \equiv \frac{i\pi}{2d}. \tag{70}$$

For the case of insulating walls, let

$$k_i \equiv \frac{2\sin(\lambda_i d)}{\lambda_i d}, \tag{71}$$

$$\gamma \equiv \sqrt{\mathrm{Ha}^2 + 4\lambda_i^2}, \tag{72}$$

$$p_{i_{1,2}} = \frac{1}{2}(\mathrm{Ha} \mp \gamma), \tag{73}$$

$$\alpha_{i_{1,2}} = \sinh(p_{i_{1,2}}). \tag{74}$$

The Fourier coefficients for velocity and induced magnetic field are then found to be

$$u_i(y) = \frac{k_i}{\lambda_i^2}\left[1 - \frac{f_i(y)}{f_i(1)}\right], \tag{75}$$

$$b_i(y) = \frac{k_i}{\lambda_i^2}\left[\frac{g_i(y)}{f_i(1)}\right], \tag{76}$$

where

$$f_i(y) = \alpha_{i_2}\cosh(p_{i_1} y) - \alpha_{i_1}\cosh(p_{i_2} y), \tag{77}$$

$$g_i(y) = \alpha_{i_2}\sinh(p_{i_1} y) - \alpha_{i_1}\sinh(p_{i_2} y). \tag{78}$$

Due to (67), derivation of (69) and (76) gives the current density components as

$$j_y = -\frac{1}{\mathrm{Ha}}\sum_{i=1,3,5}^{\infty} b_i(y)\lambda_i \sin(\lambda_i z), \tag{79}$$

$$j_z = -\frac{1}{\mathrm{Ha}}\sum_{i=1,3,5}^{\infty} \frac{\partial b_i(y)}{\partial y}\cos(\lambda_i z), \tag{80}$$

with

$$\frac{\partial b_i(y)}{\partial y} = \frac{k_i}{\lambda_i^2}\left[\frac{\partial g_i(y)/\partial y}{f_i(1)}\right], \tag{81}$$

$$\frac{\partial g_i(y)}{\partial y} = p_{i_1}\alpha_{i_2}\cosh(p_{i_1} y) - p_{i_2}\alpha_{i_1}\cosh(p_{i_2} y), \tag{82}$$

The flow rate Q is found by integrating the velocity profile over the cross section,

$$Q = 2d\sum_{i=1,3,5}^{\infty} \frac{k_i^2}{\lambda_i^2}\left[1 - \frac{F_i(1)}{f_i(1)}\right], \tag{83}$$

where

$$F(1) = \int_0^1 f(y)\,\mathrm{d}y. \tag{84}$$

For large values of γ, both numerators and denominators in (75), (76), (83) and (81) grow exponentially, and this can cause numerical problems in the evaluation. This is avoided if both numerators and denominators are multiplied by the factor $\mathrm{e}^{-\gamma}$, and expanded in sums of exponential terms.

In analogy with the expressions for current density, expressions for the wall-normal velocity gradient at the wall can be obtained through derivation of (68). This gives analytic values for the wall shear stress.

The solution for conducting Hartmann walls is obtained if (74) is replaced by

$$\alpha_{i_{1,2}} = c_h\, p_{i_{1,2}}\cosh(p_{i_{1,2}}) + \sinh(p_{i_{1,2}}), \tag{85}$$

where c_h depend on the conductivity of the Hartmann walls. The last term can be dropped for large c_h, and c_h then disappears from the solution equations.

References

[1] B.E. Launder, D.B. Spalding, The numerical computation of turbulent flows, Comput. Methods Appl. Mech. Engrg. 3 (1974) 269–289.
[2] J.A. Shercliff, A Textbook of Magnetohydrodynamics, Pergamon Press, Oxford, 1965.
[3] L. Bühler, Magnetohydrodynamic flows in arbitrary geometries in strong, nonuniform magnetic fields – a numerical code for the design of fusion reactor blankets, Fusion Technol. 27 (1995) 3–24.
[4] A.G. Kulikovskii, Slow steady flows of a conducting fluid at large Hartmann numbers, Fluid Dynam. 3 (1) (1968) 1–5.
[5] S. Aleksandrova, Buoyant convection in cavities in a strong magnetic field, Ph.D. Thesis, Coventry University, Coventry, UK, August 2001.
[6] T. Tagawa, G. Authié, R. Moreau, Buoyant flow in long vertical enclosures in the presence of a strong horizontal magnetic field. Part 1. Fully-established flow, Eur. J. Mech. B Fluids 21 (2002) 383–398.
[7] L. Leboucher, Monotone scheme and boundary conditions for finite volume simulation of magnetohydrodynamic internal flows at high Hartmann number, J. Comput. Phys. 150 (1999) 181–198.
[8] U. Müller, L. Bühler, Magnetofluiddynamics in Channels and Containers, Springer, 2001.